Two-proton spectroscopy of low-lying states in ^{17}Ne

M. J. Chromik,[1,3] P. G. Thirolf,[3] M. Thoennessen,[1,2] B. A. Brown,[1,2] T. Davinson,[4] D. Gassmann,[3] P. Heckman,[1] J. Prisciandaro,[1] P. Reiter,[3] E. Tryggestad,[1] and P. J. Woods[4]

[1]*National Superconducting Cyclotron Laboratory, Michigan State University, East Lansing, Michigan 48824*

[2]*Department of Physics and Astronomy, Michigan State University, East Lansing, Michigan 48824*

[3]*Sektion Physik, Ludwig-Maximilians-Universität München, D-85748 Garching, Germany*

[4]*Department of Physics, University of Edinburgh, Edinburgh EH9 3JZ, United Kingdom*

(Received 30 May 2002; published 12 August 2002)

The decay of the first two excited states of ^{17}Ne ($I^\pi = \frac{3}{2}^-$, $\frac{5}{2}^-$) has been studied via intermediate energy Coulomb excitation of a radioactive ^{17}Ne beam on a ^{197}Au target using a particle detector setup allowing a kinematically complete detection of the reaction products. Despite the first excited state being bound to single proton emission but unbound with respect to two proton emission, no evidence for a simultaneous two proton decay competing with the known γ decay of the $\frac{3}{2}^-$ state could be observed. The $\frac{5}{2}^-$ state decays via sequential two-proton emission to the ground state of ^{15}O. The transition matrix elements $B(E2, \frac{1}{2}^- \rightarrow \frac{3}{2}^-) = 66^{+18}_{-25}\ e^2\,\mathrm{fm}^4$ and $B(E2, \frac{1}{2}^- \rightarrow \frac{5}{2}^-) = 124(18) e^2\,\mathrm{fm}^4$ have been deduced. From the nonobservation of the simultaneous two-proton emission of the $\frac{3}{2}^-$ state a lifetime limit $\tau_{2p} > 26$ ps could be deduced in agreement with recent theoretical calculations.

DOI: 10.1103/PhysRevC.66.024313 PACS number(s): 23.50.+z, 25.60.−t, 27.20.+n

I. INTRODUCTION

The proton dripline represents one of the fundamental limits for the existence of nuclei. Nuclei beyond the proton dripline are energetically unstable with respect to the emission of a proton. Proton decays (or proton radioactivity) can be also observed in nuclei which are particle stable, if the emission of the proton occurs from an excited or isomeric state. Lifetime measurements of proton emitters grant access to detailed spectroscopic information. In contrast to the situation of α emitters, the proton decay does not contain the complication of a preformation factor. Thus the lifetime of a proton emitter depends on the spectroscopic factor together with the nuclear potential built up by the nuclear, the Coulomb, and the centrifugal barrier. The centrifugal barrier gives a strong l dependence to the lifetime and thus provides information on the single particle state occupied by the emitted proton [1].

The availability of radioactive beam facilities opened up a way to investigate two-proton decay modes. Already in 1960 Goldansky [2] predicted the existence of a two-proton decay mode which might be observable in nuclei beyond or close to the proton dripline. The two-proton decay might proceed via two possible mechanisms [3]: a sequential $2p$ decay, where two protons are emitted sequentially via an intermediate state, and a simultaneous $2p$ decay, where no (narrow) intermediate state is involved in the decay process. The simultaneous decay may proceed via an uncorrelated (''democratic'') emission of two protons, or a correlated (''diproton'') emission, where a ^{2}He cluster with strong proton-proton correlations is emitted. The democratic decay might be associated with the sequential decay through a very broad intermediate state.

Since its prediction, many experiments were aimed at the identification of a simultaneous two-proton emission in one of the rare situations, where a nucleus is stable against the emission of one proton but unstable against the emission of two protons. However, until recently none of these experiments, such as the breakup of ^{6}Be [4] and ^{12}O [5,6] or β-delayed two-proton emissions [7], could rule out the sequential decay mode via excited states in the intermediate nuclei. Apparently in all cases where it is energetically favored the decay will entirely proceed via the intermediate states, as illustrated by the (sequential) $2p$ decay of the 2^+_2 state in ^{14}O through the first excited state in ^{13}N ($1/2^+$) [8]. The first identification of the two-proton decay mode was achieved in a recently reported experiment, where evidence for a simultaneous emission of two protons from a resonance in ^{18}Ne was observed [9].

The proton dripline nucleus ^{17}Ne represents another promising candidate for a simultaneous two-proton emitter. ^{17}Ne is particle stable in the ground state, while the first excited identified state ($J^\pi = \frac{3}{2}^-, E^* = 1.288$ MeV [10]) is bound by 169 keV with respect to the emission of one proton but unbound by 344 keV relative to the emission of two protons [11]. Therefore this state can potentially decay via a simultaneous two-proton emission to the ground state of ^{15}O, since the lowest states in the intermediate nucleus ^{16}F are energetically located well above the first excited state in ^{17}Ne and their widths are too small ($\simeq 40$ keV) for a sequential decay via their tails [11] (see Fig. 1). However, the two-proton decay from the first excited state has to compete with the γ decay to the ground state in ^{17}Ne, while the higher-lying excited states in ^{17}Ne will decay sequentially through states in the intermediate nucleus ^{16}F. Thus it is necessary to combine γ spectroscopic information with two-proton spectroscopy to extract the excitation and decay properties of the low-lying states in ^{17}Ne. The γ decay of the first excited $\frac{3}{2}^-$ state has been observed in Ref. [12] with a cross section of $\sigma_{exp, \frac{3}{2}^-} = 12.0^{+5.3}_{-3.9}$ mb, thus exhausting only about half of the excitation cross section of $\sigma_{\mathrm{theo}} = 28 \pm 6$ mb theoretically predicted using the virtual photon

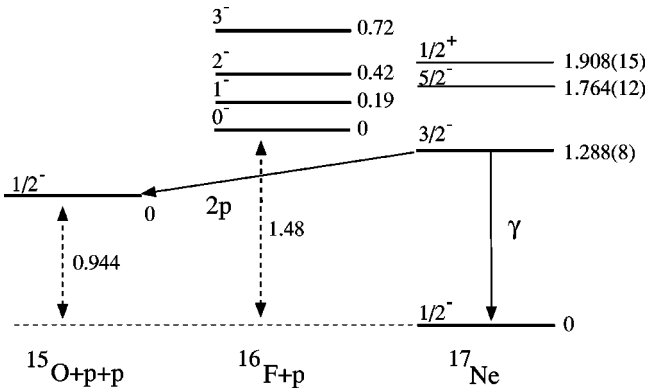

FIG. 1. Level scheme of the low-lying states in ^{17}Ne, ^{16}F, and ^{15}O. From the first excited state in ^{17}Ne an open decay channel for a simultaneous $2p$ decay exists, which is in competition with the γ decay back to the ground state in ^{17}Ne.

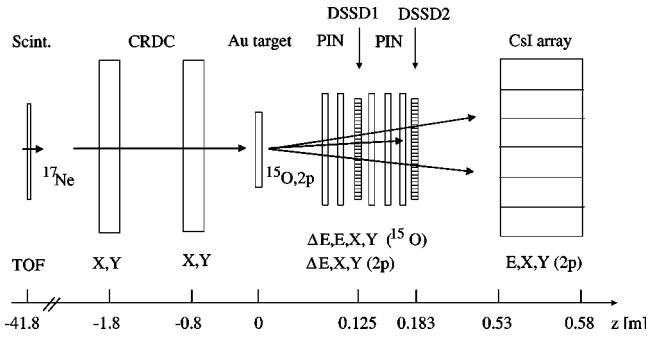

FIG. 2. Sketch of the experimental setup designed for the kinematically complete detection of all reaction products following the intermediate energy Coulomb excitation of ^{17}Ne. The ^{17}Ne projectiles were identified via a time-of-flight measurement and tracked in two cathode readout drift chambers (CRDC). The reaction products following the decay of the excited projectiles were detected in a multiple stage particle telescope, consisting of fourfold segmented PIN diodes, double sided silicon strip detectors, and an array of CsI crystals (for details see text).

method for intermediate energies following Ref. [13]. This difference could either be due to an overprediction of the $B(E2)$ values calculated within the shell model approach [12] or be interpreted as an indication for a strong potential simultaneous $2p$ decay branch. This served as a motivation for the present experiment designed for a direct search of a potential two-proton decay branch. While this measurement can yield information on the $2p$ decay cross section, a combination with the γ spectroscopy results is needed for the extraction of transition probabilities.

II. EXPERIMENTAL SETUP AND PROCEDURE

The experiment was performed at the National Superconducting Cyclotron Laboratory at Michigan State University. The radioactive ^{17}Ne beam with 58.7 MeV/nucleon was produced in a fragmentation reaction of a 100 MeV/nucleon ^{20}Ne primary beam bombarding a 790 mg/cm^2 ^{9}Be target.

The secondary beam was selected using the A1200 fragment separator [14]. In the second dispersive intermediate focus an achromatic plastic wedge equivalent to 233 mg/cm^2 Al was used to further purify the beam. The purity of the ^{17}Ne beam achieved at the focal plane was limited to 7.5% with ^{15}O as the dominant contamination (85%). Thus the largest beam contamination was identical with the reaction product to be identified. By using the Wien filter of the Reaction Product Mass Separator (RPMS) [15] the secondary beam was further purified to $\simeq$90% of ^{17}Ne. The available beam intensity was up to 20 000 particles/s. In order to reconstruct the decay energy spectrum in the center of mass system it was necessary to measure the energies and the trajectories of all reaction products.

Figure 2 shows a schematic drawing of the detector setup. The ^{17}Ne particles were identified event by event by time of flight measurements with respect to a plastic scintillator $\simeq$40 m upstream of the target. Two position sensitive cathode readout drift chambers (CRDC [16]) were placed in front of the target to track the incoming ^{17}Ne beam, which then impinged on a 112-mg/cm^2-thick ^{197}Au target. The reaction products (predominantly ^{15}O and protons) were identified in a multiple stack particle telescope, designed to simultaneously identify and track heavy and light reaction products. Two fourfold segmented PIN diodes (each 500 μm thick) were used for a ΔE measurement in front of a 1-mm-thick double sided silicon strip detector (DSSD) used for the reconstruction of the particle trajectories. Three subsequently placed fourfold segmented PIN diodes with an integral thickness of 2 mm were used to stop the ^{15}O fragments. The sum of their energy loss signals was used as an energy measurement of the ^{15}O reaction products. The use of segmented PIN diodes allowed us to accept the maximum available beam current. land would then be detected in a second 1-mm-thick DSSD and finally stopped in an array consisting of 6×6 CsI crystals ($1.7\times1.7\times5$ cm) read out by photodiodes. The second DSSD was used for the energy loss measurement and for the tracking of the outgoing protons. In addition the signal of the first DSSD was split and fed into branches with two different gain settings. The low gain setting was used to detect the ^{15}O reaction products, while the high gain setting allowed for a second position measurement of the protons. The first DSSD was placed 12.5 cm, the second one 18.3 cm behind the target. Since the CsI array had a distance of 53 cm from the target, the individual CsI crystals were covering an opening angle of $\theta=1.7°$. Thus three position measurements behind the target could be used to determine the interaction point in the target complementary to the tracking of the incoming beam with the CRDC detectors. The ''backward tracking'' of the protons could also be used to determine the breakup position of the projectiles along the beam axis as will be discussed later.

The particle telescope was calibrated using secondary beams at several energies produced by the same primary beam ^{20}Ne that was used for the production of the ^{17}Ne beam. The degrader wedge between the dipoles of the fragment separator was removed providing a variety of isotopes for the energy calibration of the fragment detectors, spanning the whole energy range of interest. The calibration of the proton detectors was performed using protons produced in

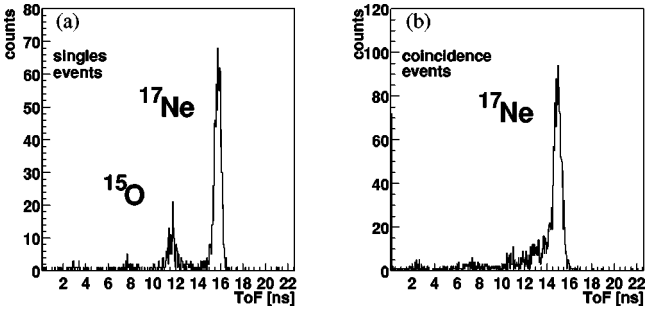

FIG. 3. Time-of-flight spectra: In panels (a) and (b) the time-of-flight spectrum is shown gated on events in the first PIN diode (PIN1). Part (a) shows the spectrum gated on down-scaled single events still containing a remaining contaminant of ^{15}O, while part (b) displays the same spectrum gated on coincidences between fragments and protons. For each trigger type (coincidences, down-scaled singles) the time-of-flight gate on incoming ^{17}Ne projectiles was derived from the corresponding spectra.

the same way with different magnet settings for the fragment separator.

A maximum current of 60 pnA for the ^{20}Ne primary beam resulted in a maximum ^{17}Ne beam intensity of 2×10^4 pps. Data were taken for about 85 h and a total of 3.25×10^7 events were recorded. Trigger conditions required either a coincidence between a signal in the first PIN diode and in the CsI array or a singles signal in the first PIN diode, scaled down by a factor of 300.

III. DATA ANALYSIS

A. Identification of the reaction channel

The ^{17}Ne projectiles were identified by time-of-flight measurements between the timing scintillator and the first PIN diode (PIN1) as described above. Figure 3(a) shows the measured time-of-flight spectrum for singles events registered with PIN1. The ^{17}Ne projectiles can easily be separated from the remaining ^{15}O contamination. Figure 3(b) shows the time-of-flight spectrum for fragment-proton coincidence events, thus suppressing the ^{15}O contribution.

The identification of the ^{15}O reaction products is demonstrated in Fig. 4, via a ΔE-E measurement. The dominant structure visible around $\Delta E\sim105$ MeV represents breakup reactions in the detector material as well as the contribution from nonreacting ^{17}Ne projectiles. ^{15}O fragments originating from reactions in the target can be identified according to their energy loss as indicated by the small dashed rectangle.

However, this condition alone cannot serve as a clean identification of reactions in the target, since breakup reactions in the first PIN diode produce a large background within the area surrounded by the dotted rectangle, which overlaps with the region where ^{15}O reaction products originating from the target are expected. The extension of the ΔE-E conditions is determined by the momentum spread of the beam of $\Delta P/P=3\%$ and by the straggling of the energy loss in the target and in PIN1, respectively. Only due to the tracking capabilities of the present experimental setup an additional selection criterion can be derived (as discussed in the following Sec. III B) allowing us to identify the event signature originating from target reactions.

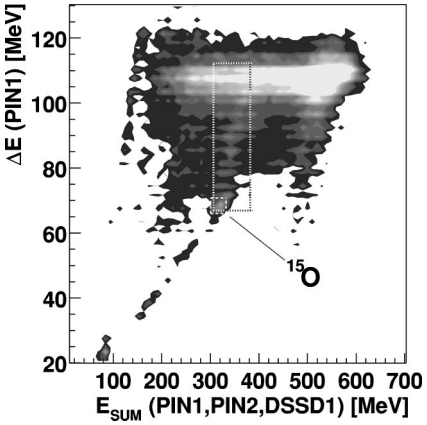

FIG. 4. Identification of the ^{15}O reaction products. The energy loss in the first PIN diode (PIN1) is plotted versus the sum of the energy deposited in the first three detectors (PIN1, PIN2, DSSD1). The component corresponding to the ^{15}O reaction products originating from the target could be identified at the expected position (marked by the dashed rectangle). The dotted rectangle corresponds to events, where the ^{17}Ne breaks up in the first PIN diode. The dominant structure visible around $\Delta E\sim105$ MeV represents breakup reactions in the detector material and the contribution from nonreacting ^{17}Ne projectiles.

In order to identify the protons emitted after the breakup of ^{17}Ne, the energy loss of the light ejectiles was measured in the second DSSD (DSSD2), while their total energy was registered in the CsI array. Figure 5 demonstrates the identification of two-proton hits. The figure shows the sum of the energy loss signals in the second DSSD (ΔE_{SUM}) versus the

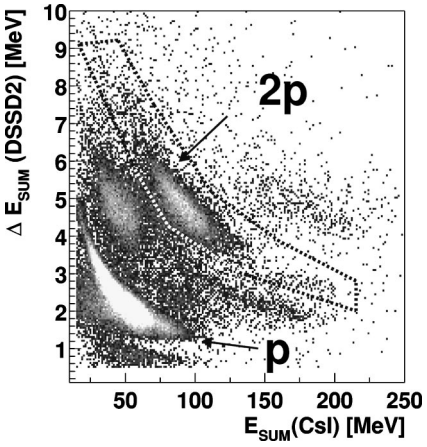

FIG. 5. Plotted is the sum of the energy loss in the second DSSD ΔE_{SUM} versus the energy deposited in the CsI array E_{SUM} in coincidence with ^{17}Ne projectiles in the entrance channel and with the identification of ^{15}O reaction products. Three bands can be identified, the most intense one corresponding to single proton events. At twice the values for ΔE_{SUM} and E_{SUM} the $2p$ band is visible, marked by the dashed polygon. A third band located in between the first two corresponds to events in which two protons were detected in the DSSD, but only one in the CsI array, which was covering a narrower opening angle.

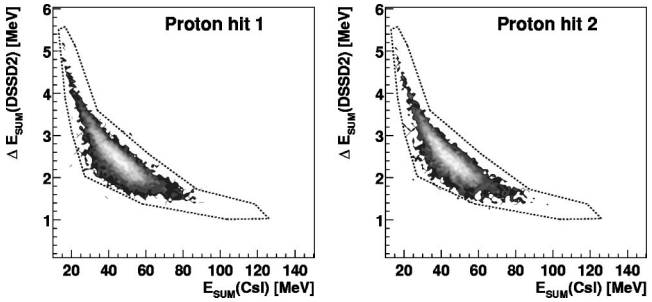

FIG. 6. The two panels show the ΔE-E spectra for each of the two protons detected in one event, revealing bands comparable to the proton band marked in Fig. 5. The dashed polygons mark the analysis conditions used for the identification of the individual protons in one event.

sum energy deposited in the CsI array (E_{SUM}) for events in coincidence with identified ^{15}O fragments. It is possible to identify an intense band corresponding to proton signals (labeled with p). Two-proton events should appear at twice the values for sum energy and energy loss of the single proton band. Indeed, the area labeled with ''$2p$'' enclosed by the dashed polygon in Fig. 5 shows evidence for $2p$ events. A third band located in between the previous ones can be seen, corresponding to events where both protons were identified in the DSSD, but only one of them was registered in the CsI array due to the smaller solid angle coverage of the CsI array compared to the DSSD.

Having identified the two-proton events, the position measurement in the second DSSD (DSSD2) could be correlated with the position measurement in the CsI array in order to assign a trajectory and a sum energy value to each of the protons. Figures 6(a) and 6(b) show the ΔE-E spectra for each of the two protons together with the analysis condition used for the proton identification (marked by the dashed polygons).

The main challenge remained in the discrimination between background events from breakup reactions in the detector material (i.e., ^{17}Ne projectiles breaking up in the detector material either due to Coulomb or nuclear excitation) and valid events originating from the target. This dominant source of background events shows almost the same energy loss and sum energy signals compared to reactions in the target. Thus the reconstruction of the particle trajectories represents the crucial prerequisite allowing us to determine the location of the reaction point on the beam axis.

B. Reconstruction of the particle trajectories

Due to efficiency losses in the tracking detectors (CRDC1/2) in front of the target for a large fraction of the events no direct extrapolation of the projectile trajectories could be applied in order to determine the interaction point on the target. However, nonreacting ^{17}Ne projectiles could be used to determine the propagation of the phase space ellipsoid between the two CRDC detectors and the first strip detector after the target, thus requiring just one position measurement in front of the target. Figure 7 demonstrates the principle for this ''drift ellipsoid method.'' Singles events

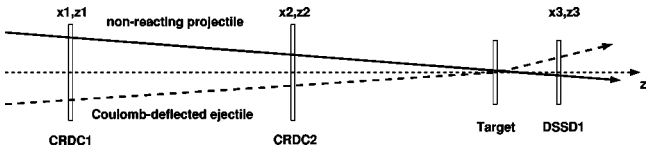

FIG. 7. This sketch demonstrates the principle of the drift ellipsoid method used to determine the interaction point in the target as described in the main text. In order to determine the properties of the incoming ^{17}Ne singles events were used, where the projectiles did not react in the target and followed a straight path as indicated by the solid line. The knowledge about the beam properties (i.e., the relation between projectile position and slope) could then be used to reconstruct the target position of the deflected particle with only one position measurement in front of the target.

from nonreacting ^{17}Ne were used for the determination of the beam properties, represented by the straight line in Fig. 7. For those events their x and y positions measured in the two CRDC's were considered together with the x and y positions determined in the first DSSD. Separately for each CRDC and each coordinate the divergence of the beam was determined, i.e., the angular deviation between the measured particle trajectory and the axis formed by the centers of the CRDC and the DSSD. Plotting this divergence as a function of the measured particle position at the CRDC resulted in the phase space ellipsoid as shown in Fig. 8(a) for the case where CRDC1 and DSSD1 were used for the tracking procedure. A linear function was fitted to the ellipsoid resulting in a fixed relation between the divergence angle and the position of the beam that could be used for the particle tracking. For those events where the ^{17}Ne projectile reacted in the target and the ejectile was deflected prior to its detection in DSSD1, the particle position in the CRDC had to be measured and the divergence angle had to be taken from the fit function derived from the singles events, allowing for an extrapolation to the interaction point in the target. Hence this drift ellipsoid method enabled the determination of the projectile trajectory even in those cases where position information was available only from one of the two CRDC detectors in front of the target.

An impression of the achievable accuracy for the determination of the interaction point at the target position can be obtained from the comparison of the difference between ex-

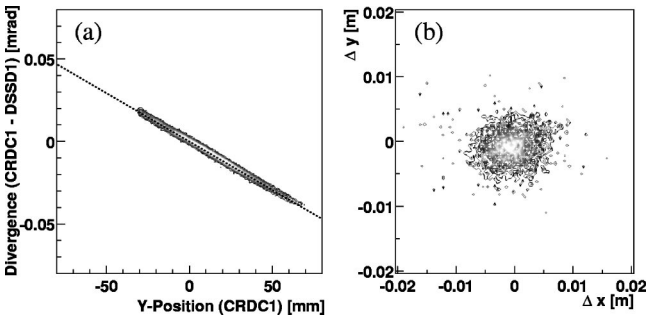

FIG. 8. Result of the ''drift ellipsoid'' method. Part (a) shows a typical phase space ellipsoid measured with the first CRDC and DSSD1. Part (b) displays the difference between the extrapolated and measured particle position in DSSD1.

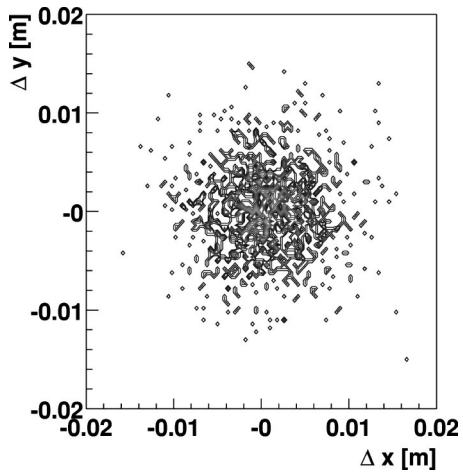

FIG. 9. Difference in each dimension between the position of the interaction point on the target as determined via ''forward tracking'' in front of the target and ''backward tracking'' with the position sensitive detectors behind the target (the latter averaged over the three available tracking combinations).

trapolated and measured position at the first DSSD as determined using nonreacting ^{17}Ne projectiles, illustrated in Fig. 8(b). The uncertainties of the x and y position as determined from a Gaussian fit were $\Delta x \sim 3.6$ mm and $\Delta y \sim 2.6$ mm, respectively.

One of the essential features of the experimental setup is the redundancy in the tracking capabilities for reaction products using position measurements in the two double-sided strip detectors and, although with reduced accuracy, with the CsI array. This offered the opportunity to use all three combinations of these detectors for independent trajectory reconstructions. Especially in those cases, where the influence of the detection of heavy fragments in the first DSSD prevented the position measurement of one or both protons, it was still possible to reconstruct their trajectories using the second DSSD and the CsI array.

Figure 9 gives a comparison of the tracking methods before and behind the target. For each coordinate the difference of the calculated positions of the interaction points obtained by the two methods was plotted. The distribution is centered around a position located at $(x,y)=[0.80(46)$ mm, $0.10(42)$ mm$]$. For the final determination of the interaction point on the target the weighed average of all backward-tracking and forward-tracking results was taken.

Finally the discrimination between the background contribution from breakup reactions in the detector material and valid events from target reactions had to be performed. This was achieved by exploiting the trajectory information of the protons allowing us to determine the breakup position along the z axis. The crossing point of the two-proton trajectories was calculated for the xz and the yz plane and the average of the two z coordinates was identified with the interaction point.

Figure 10 shows the spectrum of the breakup position along the beam axis determined from the measured proton coordinates in the second DSSD and in the CsI array. By applying a gate on energy losses corresponding to breakup

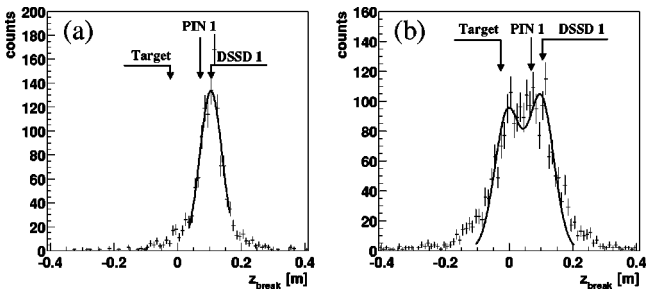

FIG. 10. Measured breakup position of the excited ^{17}Ne projectiles along the beam axis. Part (a) is gated on energy loss signals corresponding to events originating from the first PIN diode, part (b) from reactions in the target. Part (b) still shows a large remaining contribution from reactions in the first PIN diode. The solid curve is a fit using Gaussian line shapes. The arrows indicate the position of the target, the first PIN diode, and the first DSSD, respectively.

reactions in the first PIN diode, the resulting peak centers around $z \simeq 10$ cm [Fig. 10(a)], in agreement with the distance of the first detector from the target. If alternatively energy loss values corresponding to breakup reactions in the target were selected, the spectrum in Fig. 10(b) shows two components, one around $z \simeq 0$ cm originating from reactions in the target, but still with a strong admixture from breakup reactions in the first PIN diode ($z \simeq 10$ cm) as discussed before. Hence neither the energy loss condition nor the condition on the reaction coordinate can individually provide a clear separation between the two reaction types, however, combined in a two-dimensional matrix an analysis condition could be derived that clearly selected valid events originating from reactions in the target, as can be seen in Fig. 11. The dotted polygon surrounds the region of events originating from target reactions, while the dashed rectangle marks breakup reactions in the first PIN diode (PIN1). The location of the target and PIN1 on the z axis is additionally indicated.

C. Decay energy spectrum

After the identification of the reaction channel the measured four-momenta of the reaction products (^{15}O, two protons) had to be transformed into the center-of-mass system, resulting in the decay energy spectrum with respect to the mass of ^{15}O(g.s.) and two protons as shown by the histogram in the upper part of Fig. 12. It reveals a prominent peak at around 900 keV, while no evidence for a peak around a decay energy of 344 keV could be found, which would be the expected transition energy for a simultaneous $2p$ decay. With the complete and redundant tracking capabilities of the present experimental setup previously reported intensity in this energy region [17] could be identified with background reactions in the detector material. The lower part of Fig. 12 again displays the decay energy spectrum, but this time accumulated only for those events where the particle tracking information from both DSSD's could be used to derive the breakup position, resulting in a much more restrictive analysis condition. Here no contribution around 300 keV remains at all.

The peak around $E_{\mathrm{decay}} = 900$ keV can be attributed to transitions from the excited $\frac{5}{2}^-$ state in ^{17}Ne at an excitation

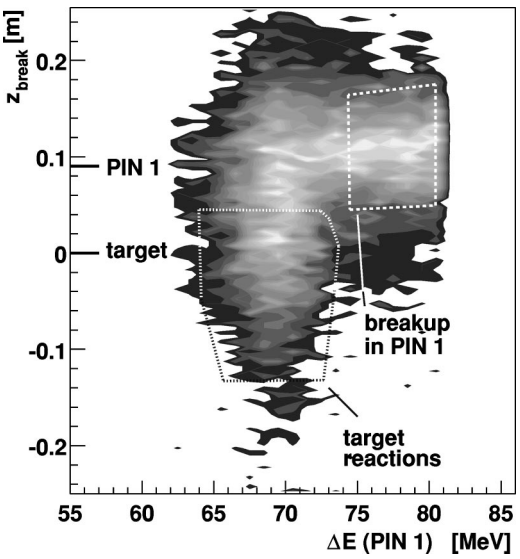

FIG. 11. Determination of the analysis gate for breakup reactions in the target. Plotted is the measured breakup position of the excited ^{17}Ne projectiles along the z axis versus the energy loss of the heavy fragment in the first PIN diode (limited to 80 MeV for presentation purposes). An intensity enhancement around the target position (0 cm) and energy loss values corresponding to ^{15}O fragments originating from target reactions can be seen. Two-dimensional conditions for the selection of reactions in the target (dotted polygon) and for reactions in the first PIN diode (dashed rectangle) were derived from the known positions and respective energy loss values.

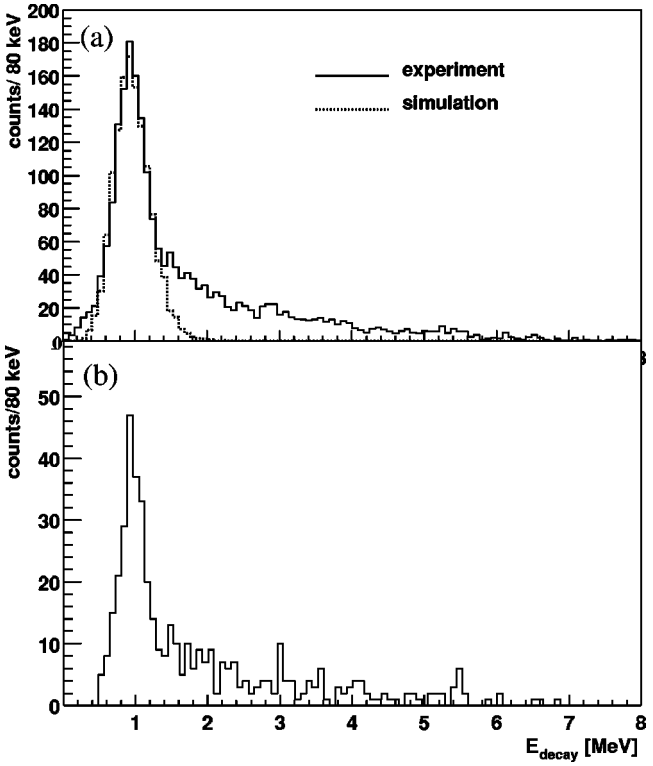

FIG. 12. Upper panel: reconstructed decay energy spectrum for the breakup of Coulomb-excited ^{17}Ne projectiles relative to the mass of ^{15}O and two protons. The histogram represents the measured decay energy spectrum. The dashed histogram corresponds to the simulated spectrum as discussed in the main text. Bottom panel: same spectrum as in the upper part, but accumulated only for events where the tracking information from both DSSD's could be used, resulting in a more restrictive analysis condition for the breakup position compared to the upper part.

energy of 1764(12) keV. Transitions from higher-lying excited states may also be present, but either they cannot be resolved or suffer from the decreasing detection efficiency at higher decay energies.

Figures 13(a) and 13(b) depict the individual decay step energies for events with a decay energy between 620 and 1220 keV. The decay step energy was obtained by adding the decay energy of an individual proton to the corresponding recoil energy. The decay step energies were sorted in a way that panel (a) contains the larger decay energy and panel (b) the smaller one. With a Gaussian fit values of 609 ± 10 and 301 ± 5 keV for the individual decay energies of the two protons were obtained. Thus the decay from the $\frac{5}{2}^-$ state in ^{17}Ne shows clear evidence of a sequential $2p$ decay. This is supported by the opening angle distribution of the two protons in the center-of-mass system as displayed in Fig. 14(b). It reveals an isotropic distribution as expected for a sequential decay. In addition, Fig. 14(a) shows the measured Coulomb deflection angle in the center-of-mass system for the same event class, clearly indicating that Coulomb excitation, dominant at small deflection angles, prevailed over potential nuclear excitations, which would have led to larger deflection angles.

D. Monte Carlo simulations

In order to be able to compare the previously measured γ-ray strength for the decay of the first excited state [12] with the observed $2p$-strength of this experiment and aiming at the extraction of the excitation cross sections for the first and second excited state it is necessary to ensure that in each case Coulomb excitation is the dominant excitation mechanism.

While in a typical intermediate energy γ-spectroscopy experiment after Coulomb excitation it is sufficient to limit the angular acceptance for the detection of the Coulomb-deflected projectiles, thus selecting a minimum impact pa-

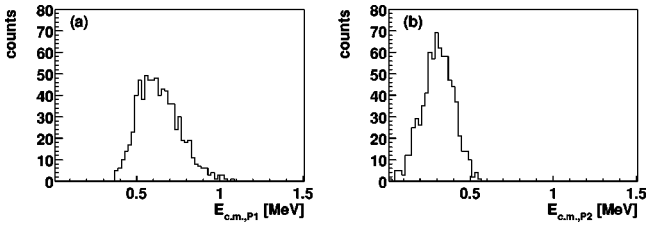

FIG. 13. Energies of the two decay steps of the sequential $2p$ decay derived from the individually measured proton energies leading to the 900-keV decay energy peak of Fig. 12. Plotted is the decay energy attributed to the emission of each proton corrected for the recoil energy of the ^{15}O fragment. Panel (a) shows the energy for the proton with the higher energy, while panel (b) contains the protons with the lower decay energies.

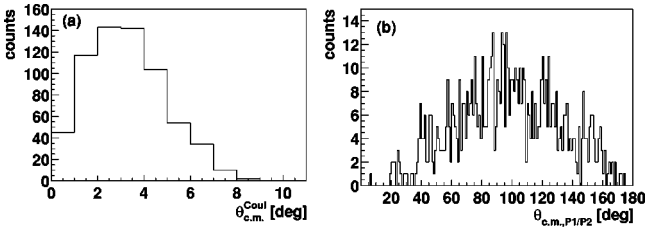

FIG. 14. (a) Measured Coulomb deflection angles for events originating from the peak around $\simeq 900$ keV in the center-of-mass decay energy spectrum (Fig. 12). (b) Opening angles of the two protons contributing to the 900-keV peak, showing an isotropic distribution characteristic for a sequential $2p$ decay.

rameter, in order to restrict potential nuclear excitations to a negligible amount, the breakup of the excited ^{17}Ne projectiles in the present experiment requires a more quantitative understanding. This includes the determination of the detection and analysis efficiency, which was achieved via Monte Carlo simulations. Ingredients to the simulation code were the reaction mechanism (sequential or simultaneous two-proton decay), excitation energies and widths of the first excited states, and the Coulomb deflection process in the target. Also included in the simulation procedure were the angular straggling of the reaction products in the detectors, the measured detector responses, the measured beam properties and the geometric efficiency of the setup (for details see Ref. [18]). Figure 15(a) shows the simulated efficiency for detecting events with a given Coulomb deflection angle, starting from an isotropic distribution. The efficiency for detecting events with Coulomb deflection angles of $\theta^{Coul}_{\mathrm{c.m.}} > 6°$, corresponding to impact parameters of smaller than 14 fm (compared to 11.2 fm for the ''touching spheres'' geometry [19]) is smaller than 10%.

In addition Fig. 15(b) shows the measured $\theta^{Coul}_{\mathrm{c.m.}}$ distribution, allowing us to conclude that Coulomb excitation is the dominant excitation process.

In order to reproduce the decay energy spectrum shown in Fig. 12, decays from the $\frac{5}{2}^-$ and from the $\frac{5}{2}^+$ state were included in the simulation. While the $\frac{5}{2}^+$ state (with its known excitation energy of 2651 keV [10]) was included only to reproduce the tail of the $\frac{5}{2}^-$ state correctly, a χ^2 minimization procedure was used to determine the measured excitation energy of the $\frac{5}{2}^-$ state, resulting in 1900(78) keV. Implications of the difference of this finding with the level energy for the $\frac{5}{2}^-$ state given by Ref. [10] as 1764(12) keV will be discussed in Sec. IV A.

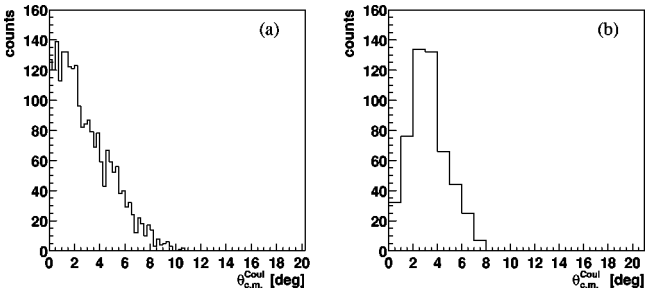

FIG. 15. Coulomb deflection angle (a) simulated for an isotropic angular starting distribution and (b) measured distribution.

The simulated decay energy spectrum is represented by the dotted line overlaying the histogram in Fig. 12.

E. Lifetime limit for the simultaneous $2p$ decay

From the energy spectrum in Fig. 12 it can be concluded that less than one simultaneous two-proton transition from the first excited $\frac{3}{2}^-$ state in ^{17}Ne could be observed in the present experiment. The comparison of this experiment with the γ spectroscopy experiment of Ref. [12] results in an upper limit for the branching ratio $\Gamma_{2p}/\Gamma_\gamma$ and thus in a lower lifetime limit for the simultaneous $2p$ decay for the $\frac{3}{2}^-$ state. Taking into account the different numbers of registered ^{17}Ne projectiles and virtual photons in the Coulomb excitation process as well as the respective target thicknesses and detection efficiencies leads to a factor of 1.73 that has to be multiplied with the number of observed transitions from the $\frac{3}{2}^-$ state $N^{\mathrm{obs}}_\gamma = 86 \pm 22$ in the γ experiment. Hence $\leqslant 1$ simultaneous $2p$ transitions measured in the present experiment correspond to the observation of $148^{+47}_{-60}\gamma$ transitions that would be observable with a γ detector setup of the same efficiency and opening as the actually used particle telescope. Here the errors include the uncertainty of the efficiency in both experiments and the statistical error of the observed γ transitions. Since no counts were observed in the $2p$ branch, the upper one-sigma limit for the branching ratio has to be given. For the case, where one branch contains zero and the other n counts, the branching ratio according to Ref. [20] is given by

$$\Gamma_{2p}/\Gamma_\gamma \leqslant \frac{1-(0.32)^{1/n}}{(0.32)^{1/n}}. \tag{1}$$

With $n=148$ the branching ratio results in $\Gamma_{2p}/\Gamma_\gamma \leqslant 0.0077$ with a 1σ confidence level. Thus the simultaneous $2p$ decay from the $\frac{3}{2}^-$ state in ^{17}Ne is at least a factor of 130 slower compared to the γ decay, which is dominated by $M1$ decay.

So far no direct measurement of the $M1$ lifetime has been performed. The value needed here was calculated within the shell model using the WBP interaction by Warburton and Brown [21] and an effective $M1$ operator derived from sd-shell M1 transition data [22]. The calculated value for the $\frac{3}{2}^- \rightarrow \frac{1}{2}^-$ $M1$ transition in ^{17}Ne results to 0.20 ± 0.05 ps, where the error was estimated by comparison of the experimental values for other $M1$ transitions in ^{17}N, using the same Hamiltonian and $M1$ operator. With this value, the experimental lower limit on the branching ratio can be translated into a lower two-sigma limit for the lifetime of the simultaneous $2p$ decay of the first excited state of $\tau_{2p} > 26$ ps. This limit was derived from the strictly gated decay energy spectrum shown in Fig. 12(b). However, if the few counts around $\simeq 300$ keV in the less restrictive spectrum in Fig. 12(a) would be interpreted as background from breakup reactions in the detectors and accordingly concluded that already less than one $2p$ decay from the first excited state in ^{17}Ne was observed in Fig. 12(a), the lower limit on the lifetime could be increased by a factor of five.

TABLE I. Calculated virtual photon numbers for the transitions relevant for the extraction of experimental $B(E2)$ values. The level energies have been taken from Ref. [9].

Transition	E^* [keV]	n_{E1}	n_{E2}	n_{M1}
$\frac{1}{2}^- \rightarrow \frac{3}{2}^-$	1288		47357	30
$\frac{1}{2}^- \rightarrow \frac{5}{2}^-$	1764		24990	
$\frac{1}{2}^- \rightarrow \frac{1}{2}^+$	1908	184		
$\frac{1}{2}^- \rightarrow \frac{3}{2}^-$	1288		34881	20

F. Extraction of $B(E2)$ values

The measured cross section for the $2p$ decay of ^{17}Ne is given by

$$\sigma_{exp,2p} = \frac{N_{obs}}{\epsilon_{2p} \cdot N_T \cdot N_{^{17}\mathrm{Ne}}} \tag{2}$$

with $N_T = 3.42 \times 10^{-6}$ nuclei in the target per fm^2 and $N_{^{17}\mathrm{Ne}} = 2.05 \times 10^9$ detected ^{17}Ne projectiles. The efficiency for detecting $2p$ decays from the $\frac{3}{2}^-$ and from the $\frac{5}{2}^-$ state is $\epsilon_{2p,3/2^-} = 1.3(2)\%$ and $\epsilon_{2p,5/2^-} = 5.7(8)\%$, respectively. In the decay energy peak originating from decays of the $\frac{5}{2}^-$ state $1196 \pm 35^{\mathrm{stat.}} \pm 34^{\mathrm{syst.}}$ counts were observed, and less than one count from the $\frac{3}{2}^-$ state. Thus we measured an excitation cross section of $\sigma_{\mathrm{exp},2p,5/2^-} = 29.9 \pm 4.4$ mb for the $2p$ decays from the $\frac{5}{2}^-$ state and a limit of $\sigma_{\mathrm{exp},2p,3/2^-} < 0.011(2)$ mb for the simultaneous $2p$ decay from the first excited state in ^{17}Ne.

In order to extract the reduced transition probabilities for the excitation of the $\frac{3}{2}^-$ and the $\frac{5}{2}^-$ states of ^{17}Ne, the virtual photon method was used in the intermediate energy approach by Baur and Bertulani [13]. This approach is similar to a fully relativistic treatment, except that the Rutherford bending of the projectile trajectory is taken into account. This leads in the present case to $\simeq 5\%$ smaller virtual photon numbers compared to the relativistic approach. The virtual photon numbers relevant for the excitation process of the $\frac{3}{2}^-$ and the $\frac{5}{2}^-$ state as well as for the $\frac{1}{2}^+$ state are given in Table I. Due to their smaller uncertainties the level energies from Ref. [10] have been used.

The excitation cross section of a nuclear level via Coulomb excitation can be expressed as the product of the photoabsorption cross section $\sigma_\gamma^{\pi\lambda}$ ($\pi\lambda$ denoting the electrical or magnetic radiation characteristics of multipolarity λ) with the number $n_{\pi\lambda}$ of respective virtual photons. The total excitation cross section σ_{exc} can be obtained by summing over all allowed transitions [13]:

$$\sigma_{exc} = \sum n_{\pi\lambda} \cdot \sigma_\gamma^{\pi\lambda}. \tag{3}$$

Here the photoabsorption cross section $\sigma_\gamma^{\pi\lambda}$ is given by

$$\sigma_\gamma^{\pi\lambda} = \frac{(2\pi)^3(\lambda+1)}{\lambda[(2\lambda+1)!!]^2} \sum_f \rho_f(\epsilon) k^{2\lambda-1} B(\pi\lambda). \tag{4}$$

$\rho_f(\epsilon)$ is the density of states which in the present case is taken to be a δ function at the excitation energy of the $\frac{3}{2}^-$ and the $\frac{5}{2}^-$ state and k is the wave number. Since in the present case the two relevant final states are treated separately, no summation over final states is needed.

The $\frac{1}{2}^- \rightarrow \frac{5}{2}^-$ excitation can proceed only via $E2$ photons. However, a contribution from the neighboring $\frac{1}{2}^+$ state to the decay energy peak of Fig. 12 cannot be excluded *a priori* due to the limited energy resolution. Since no experimental data on the $B(E1, ^{17}\mathrm{Ne}, \frac{1}{2}^- \rightarrow \frac{1}{2}^+)$ is available, the upper limit for the $B(E1, ^{17}\mathrm{N}, \frac{1}{2}^- \rightarrow \frac{1}{2}^+) \leqslant 1.1 \times 10^{-4}$ $e^2\,\mathrm{fm}^2$ from Ref. [23] was used to calculate the excitation cross section. The number of virtual photons is $n_{E1} = 184$ (see Table I) which leads to an excitation cross section of $\sigma_{E1} \leqslant 0.1$ mb, which is negligible. The mirror asymmetry in the $B(E1)$ values for those nuclei should be similar to the asymmetry in the first-forbidden decay rates to the $\frac{1}{2}^+, T = \frac{1}{2}$ state which is measured to be $^{17}\mathrm{Ne}/^{17}\mathrm{N} = 1.6$ [24]. Thus $\sigma_{E1} \leqslant 0.2$ mb can be assumed for ^{17}Ne, and the measured cross section $\sigma_{exp,5/2^-} = 29.9 \pm 4.4$ mb observed in the peak in Fig. 12 can be interpreted as the result of a Coulomb excitation exclusively to the $\frac{5}{2}^-$ state followed by a sequential two-proton emission. From the virtual photon number $n_{E2} = 24\,990$ a value of $B(E2, ^{17}\mathrm{Ne}, \frac{1}{2}^- \rightarrow \frac{5}{2}^-) = 124(18) e^2\,\mathrm{fm}^4$ can be derived.

The $\frac{3}{2}^-$ state in ^{17}Ne can be excited by $E2$ or $M1$ transitions, the virtual photon numbers for the present experiment are $n_{M1} = 20$ and $n_{E2} = 34\,881$ (Table I). Since no experimental data on the $M1$ lifetime in ^{17}Ne is available, the value of $B(M1, ^{17}\mathrm{Ne}, \frac{1}{2}^- \rightarrow \frac{3}{2}^- = 0.29\ \mu^2)$ has been calculated within the shell model approach discussed in Sec. III E. This leads to an $M1$ photoabsorption cross section of $\sigma_\gamma^{M1} = (12 \pm 0.49) \times 10^{-3}$ mb, which finally results in an $M1$ excitation cross section $\sigma_{\mathrm{exc},M1} = 0.24 \pm 0.1$ mb. Compared to the measured cross section of $\sigma_{\mathrm{exp},3/2^-} = 11.9^{+3.3}_{-4.5}$ mb this contribution is small and thus will be neglected for the calculation of the $B(E2)$ value. With $n_{E2} = 34\,881$ Eq. (3) leads to $\sigma_\gamma^{E2} = 3.4^{+1.0}_{-1.3} \times 10^{-4}$ mb. Using the energy of the first excited state of 1288 keV, Eq. (4) results in a value of $B(E2, ^{17}\mathrm{Ne}, \frac{1}{2}^- \rightarrow \frac{3}{2}^-) = 66^{+18}_{-25}$ $e^2\,\mathrm{fm}^4$.

IV. DISCUSSION

Figure 16 summarizes the nuclear excitation and decay properties of ^{17}Ne measured in the present work. Individual features will be discussed in the following sections.

A. Assignment of the 1900(78)-keV transition

The dominant peak in the decay energy spectrum shown in Fig. 12 was attributed to decays from a state with a level energy of $E^* = 1900(78)$ keV and a width that could be well reproduced by simulations (see Fig. 12) assuming two-proton decays originating from a single state in ^{17}Ne. In this energy region the level scheme of ^{17}Ne, as measured by Ref. [10], shows two neighboring levels, the $\frac{5}{2}^-$ state at 1764(12) keV and the $\frac{1}{2}^+$ state at 1908(15) keV, respectively.

In the previous section it was discussed that contributions from decays of the $\frac{1}{2}^+$ state should be negligible due to its

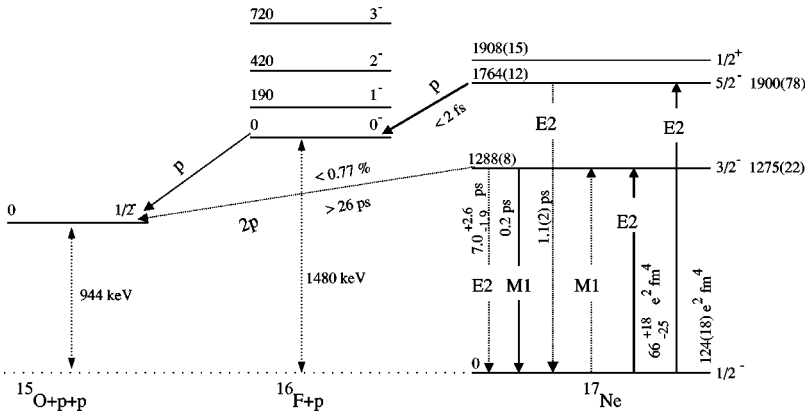

FIG. 16. Summary of the properties for the excitation and deexcitation processes for the lowest excited states in ^{17}Ne as determined in the present work.

small excitation cross section. Thus the peak in Fig. 12 was assigned to originate exclusively from decays of the $\frac{5}{2}^-$ state in ^{17}Ne. Nevertheless it remains unsatisfying that the measured value for the excitation energy of the $\frac{5}{2}^-$ state in the present work agrees only within the 2σ limit with the value measured by Ref. [10]. One possible source of a systematic error in the present experiment could be an unresolved contribution from decays of the $\frac{1}{2}^+$ state. However, even if the $\frac{1}{2}^+$ state would be populated by a factor of $\simeq$30 stronger than expected, the peak in Fig. 12 would still contain only a $\simeq$10% contribution from decays of this state, reducing the value for $E^*(5/2^-)$ only by about $\simeq$10–20 keV. Other sources of potential systematic errors are not evident. Thus the measured level energy in combination with the spin assignment derived in the present work could be considered as questioning the spin assignment from the $3n$-pickup reaction experiment by Ref. [10].

In Ref. [10] the $(\frac{5}{2}^-,\frac{1}{2}^+)$ doublet could not be resolved. A peak was observed at $\simeq$1850 keV with a width indicating about equal contributions from two states. Two states at 1764(12) keV and at 1908(15) keV were fitted to the measured peak. The quoted uncertainties correspond to the statistical errors obtained by the fit procedure as can be seen by comparing the error margins of individual states present in the same energy spectrum. The spin assignment by Ref. [10] was derived by measurements of the angular distribution and could be confirmed by calculations within the isobaric multiplet mass equation approach (IMME, Refs. [25,26]).

However, a careful reanalysis of the excitation energy spectrum given in Ref. [10] shows that the widths [full width at half maximum (FWHM)] used to fit the peaks of the $\frac{1}{2}^-$, $\frac{3}{2}^-$, $\frac{5}{2}^-$, $\frac{1}{2}^+$, and $\frac{5}{2}^+$ states were approximately 180, 195, 195, 225, and 250 keV, with their corresponding level energies of 0, 1288, 1764, 1908, and 2651 keV, respectively. The experimental energy resolution is given as 180 keV (FWHM). For ''some'' peaks above the particle threshold slightly broader widths were used [10]. A slightly broader width used to fit the doublet in order to generate a smoother excitation energy dependence of the peak width would bring the two states closer together, resulting in a higher level energy for the $\frac{5}{2}^-$ state and a lower one for the $\frac{1}{2}^+$ state. Thus the discrepancy in the $E^*(5/2^-)$ value between the present measurement and Ref. [10] could be reduced.

In summary, the present experimental results do not necessarily disagree with the level ordering for the $(\frac{5}{2}^-,\frac{1}{2}^+)$ doublet as derived by Ref. [10] and supported by the IMME calculations which also reproduce the other level energies. However, the uncertainties given for those level energies by Ref. [10] do not take into account the influence of the widths, chosen for the fit of the decay energy peak that corresponds to the $(\frac{5}{2}^-,\frac{1}{2}^+)$ doublet. Hence the quoted values seem to underestimate the realistic uncertainties for the energetic position of the $\frac{5}{2}^-$ and $\frac{1}{2}^+$ state.

B. Excitation and decay properties of the 5/2$^-$ state

A $B(E2)$ value for the $\frac{1}{2}^-\rightarrow\frac{5}{2}^-$ excitation could be extracted from the decay energy spectrum as $B(E2,^{17}\mathrm{Ne},\frac{1}{2}^-\rightarrow\frac{5}{2}^-)=124(18)e^2\,\mathrm{fm}^4$. This value will be discussed in Sec. IV D together with the $B(E2)$ value for the excitation of the $\frac{3}{2}^-$ state.

From $B(E2,^{17}\mathrm{Ne},\frac{1}{2}^-\rightarrow\frac{5}{2}^-)$ a lifetime for the $E2$ deexcitation of $\tau_{E2}=1.1(2)$ ps could be determined. Since no evidence for this transition was found in the γ experiment [12], an upper limit for the lifetime of the first decay step of the sequential $2p$ decay of the $\frac{5}{2}^-$ state in ^{17}Ne could be extracted. Considering the excitation-energy scheme given by Ref. [10] the sequential decay of the $\frac{5}{2}^-$ state in ^{17}Ne can only proceed through the 0^- or the 1^- state in ^{16}F. Since the last two protons in ^{17}Ne occupy either an (sd) or a (d^2) configuration and considering parity arguments, the decay through the 1^- state in ^{16}F would only be possible for a proton with $l=2$. With the Q value of $Q_p=94$ keV for this decay path a simple barrier penetration calculation results in a lifetime of $\simeq$300 ps, while similar calculations yield a value of $\simeq$1.4 fs for the decay through the 0^- state in ^{16}F by the emission of a proton with $l=2$. Thus the decay of the $\frac{5}{2}^-$ state has to proceed via the 0^- state. A decay through the 0^- state in ^{16}F would also be in agreement with the measured single proton energies in the center-of-mass system [Figs. 13(a), and 13(b)].

C. Lifetime for the 2p decay from the 3/2$^-$ state

In combination with the previous γ experiment [12] a branching ratio of $\Gamma_{2p}/\Gamma_\gamma\leqslant 0.0077$ for the two possible decay modes of the $\frac{3}{2}^-$ state in ^{17}Ne could be derived from the

present experiment, allowing it to be converted into a lifetime limit of $\tau_{2p}>26$ ps for the simultaneous $2p$ decay of the first excited state. The experimental lower lifetime limit obtained with the presented significantly improved experimental technique and analysis forces us to revise the interpretation of a previous $2p$-decay experiment [17,27] in which some $2p$ decay events were suggested.

This lifetime limit can now be compared to various theoretical predictions.

Theoretical models for the two-proton decay have been recently improved [3,28,29]. But we start with the simplest model [30] which was used in previous calculations [12] of the two-proton decay of the first-excited state of ^{17}Ne. This scenario assumes the penetration of a pointlike ^{2}He cluster through a Coulomb barrier for a particle of charge $Z=2$ and a core with charge $Z=8$. We obtain the width by calculating the phase shift for the scattering of a diproton from a potential of radius 3.0 fm and diffuseness of 0.6 fm with a well depth constrained to give a resonance peak at 0.344 MeV. The total orbital angular momentum for the $\frac{3}{2}^- \rightarrow \frac{1}{2}^-$ decay must be $L_{\text{total}}=2$. In the cluster model [30], the diproton is described as an *s*-state ($l=0$) and the relative angular momentum between the diproton and the $A=15$ core is $L=2$. The calculated decay width is $\Gamma=1.6\times10^{-12}$ MeV, translating into a lifetime of $\tau=0.4$ ns. The decay width depends also on the spectroscopic factor associated with the simultaneous $2p$ decay, which can be obtained from the p-sd shell-model wave functions [21]. The two-nucleon decay amplitudes obtained with the WBP and WBT wave functions are dominated by $(0d_{5/2})^2$ and $0d_{5/2}-1s_{1/2}$ components which are near unity.

In this simplest approach all of the energy (two-proton decay Q value) available for the decay is in the relative motion of the ^{2}He and ^{15}O. This model has recently been improved by Barker [28] within the *R*-matrix formalism by adding the effects of the interaction of the two protons during the decay. In this model the energy for the decay is shared between the two protons and ^{15}O. The calculated $L=2$ decay width is $\Gamma\approx5\times10^{-14}$ MeV, translating into a lifetime of 130 ns. The reduction in the rate can be understood in terms of an effective Q value for the relative motion of ^{2}He and ^{15}O which is reduced from the actual Q value for the decay. The interaction between the two protons is also included in the three-body breakup model of Grigorenko *et al.* [3,29]. The result given in Ref. [29] is $\Gamma=1.4(3)\times10^{-15}$ MeV corresponding to a lifetime of 470(100) ns.

The measured lifetime limit is in agreement with the lifetime predictions as described in the previous paragraph. In order to further investigate the simultaneous $2p$ decay of the first excited state in ^{17}Ne it would be necessary to increase the sensitivity towards larger lifetimes by orders of magnitudes. This will require much higher beam currents and newly designed experimental setups allowing a kinematical complete reconstruction of the decay accommodated to the expected longer lifetimes.

D. Reduced transition probabilities

As described in Sec. III F, $B(E2)$ values for the excitation of the two lowest-lying excited states in ^{17}Ne could be extracted. These values can be interpreted in the context of calculations within the shell model approach. Earlier calculations (partly published in Ref. [12]) overestimate the $B(E2)$ values obtained in the present work. In this earlier publication the $B(E2)$ values in ^{18}Ne and ^{17}Ne were discussed in a configuration space of $(\pi sd)^2$ for the ^{18}Ne and $(\nu p)^{-1}(\pi sd)^2$ for ^{17}Ne. The results obtained with the WBP interaction [21] are close to those expected in the approach of a weak coupling of a $p_{1/2}$ neutron hole to the states in ^{18}Ne. In the weak coupling approach (described, e.g., in Ref. [31]) the angular momentum J of the proton hole is coupled to a vibrational excitation with the angular momentum R giving rise to a multiplet of states with total angular momentum I:

$$I=|J-R|,|J-R|+1,\cdots J+R. \tag{5}$$

In the limit of weak coupling, the various nuclear moments can be expressed as a sum of contributions from the vibrational and intrinsic degrees of freedom. In this situation, only the vibrational moment contributes to such transitions and the $B(E\lambda)$ value is directly related to the vibrational transition rate:

$$B(E\lambda;RJI\rightarrow R'JI')=(2I'+1)(2R+1)\begin{Bmatrix} R & J & I \\ I' & \lambda & R' \end{Bmatrix}^2 \times B(E\lambda;R\rightarrow R'). \tag{6}$$

The sum of the transition probabilities to the different members I' of the final multiplet is equal to $B(E\lambda;R\rightarrow R')$ [31]. In the present case the $p_{1/2}$ neutron hole is coupled to the collective $0^+\rightarrow2^+$ excitation in ^{18}Ne. With $R=0$, $R'=2$, $J=\frac{1}{2}$, $\lambda=2$, $I=\frac{1}{2}$ and $I'=\frac{3}{2}$ or $I'=\frac{5}{2}$ for the $\frac{3}{2}^-$ and the $\frac{5}{2}^-$ state, respectively, the weak-coupling relationship for the $B(E2)$ values in ^{17}Ne and ^{18}Ne can be obtained from Eq. (6):

$$B(E2,^{18}\text{Ne},0^+\rightarrow2^+)=B\left(E2,^{17}\text{Ne},\frac{1}{2}^-\rightarrow\frac{3}{2}^-\right)+B\left(E2,^{17}\text{Ne},\frac{1}{2}^-\rightarrow\frac{5}{2}^-\right), \tag{7}$$

where the $B(E2)$ values to the $\frac{3}{2}^-$ and the $\frac{5}{2}^-$ states exhibit a ratio of 2:3 [12]. Thus ^{17}Ne could be interpreted in terms of the known $B(E2)$ value from ^{18}Ne. Using a Woods-Saxon potential it was also demonstrated in Ref. [12] that the smaller single-particle separation energies in ^{17}Ne compared to those in ^{18}Ne led to about a 50% increase in the $B(E2)$ values in ^{17}Ne compared to the $B(E2)$ values expected in the oscillator model.

The results obtained in the above described model space using Woods-Saxon single particle wave functions [12] are given in the second column of Table II. They were deduced with effective charges of $e_p=1.50$ and $e_n=0.65$ chosen to reproduce the $B(E2)$ value of ^{18}Ne. In addition the corresponding picture in the mirror system (^{17}Ne and ^{18}O) is listed. The predicted $B(E2)$ values for ^{17}Ne were about a factor of two larger than the values obtained in the present

TABLE II. Comparison of calculated and experimental $B(E2)$ values. The calculated values are given for two shell model calculations using different configuration spaces (see text).

Transition	Earlier theory (e^2 fm^4)	This work (e^2 fm^4)	Experiment (e^2 fm^4)
$B(E2,{}^{18}\mathrm{Ne},0^+\rightarrow 2^+)$	256	256	266(25) [34]
$B(E2,{}^{17}\mathrm{Ne},\frac{1}{2}^-\rightarrow\frac{3}{2}^-)$	151	105	66^{+18}_{-25}
$B(E2,{}^{17}\mathrm{Ne},\frac{1}{2}^-\rightarrow\frac{5}{2}^-)$	235	155	124(18)
$B(E2,{}^{18}\mathrm{O},0^+\rightarrow 2^+)$	46	46	45(2) [34]
$B(E2,{}^{17}\mathrm{N},\frac{1}{2}^-\rightarrow\frac{3}{2}^-)$	33	7.1	
$B(E2,{}^{17}\mathrm{N},\frac{1}{2}^-\rightarrow\frac{5}{2}^-)$	42	10.3	6.7(1.2) [11]

experiment, and the $B(E2)$ values for ^{17}N were almost an order of magnitude larger compared to the experiment.

The earlier shell model approach disregarded the fact that the 0^+ and 2^+ states in ^{18}Ne have large admixtures of $(\nu p)^{-2}(\nu sd)^2(\pi sd)^2$ configurations, which have a strong influence on the $B(E2)$ values. The rather large effective charges required in the earlier calculations were related to the influence of these core-excited configurations [32]. The admixture of $(\nu p)^{-3}(\nu sd)^2(\pi sd)^2$ in ^{17}Ne may not be as large, since the third neutron-hole has to go into the deeper-lying $p_{3/2}$ orbital (the respective discussion for ^{18}O and ^{17}N follows an analog pattern except that the role of protons and neutrons is reversed). The difference of the influence of the $(\nu p)^{-2}(\nu sd)^2(\pi sd)^2$ and the $(\nu p)^{-3}(\nu sd)^2(\pi sd)^2$ admixtures for ^{18}Ne and ^{17}Ne, respectively, shows up in the disagreement of the present experimental $B(E2)$ values with the theoretical values listed in the second column in Table II. Together with the discrepancy in the mirror system this can be interpreted as a breakdown of the weak coupling model applied to the restricted configuration space.

In order to quantify this effect, the full $(p_{1/2}, d_{5/2}, s_{1/2})^n$ model space was used with the REWIL Hamiltonian (the F interaction in Ref. [33]). In this model space the core excited states discussed above are explicitly included. This new theoretical approach results in the values listed in the third column of Table II. For these calculations effective charges of $e_p=1.40$ and $e_n=0.40$ are chosen to reproduce the $A=18$ values within the experimental uncertainties. The overall agreement between the experimental and theoretical $B(E2)$ values for $A=17$ and $A=18B(E2)$ are much improved when these core excited states are taken into account. These results illustrate the limitations of the weak coupling approach, stressing the necessity of a careful consideration of the configuration space.

V. CONCLUSION

In conclusion we studied the excitation and decay of the low-lying $\frac{3}{2}^-$ and $\frac{5}{2}^-$ states in ^{17}Ne using the intermediate energy Coulomb excitation combined with $2p$ spectroscopy. The results were analyzed in combination with a previously performed γ spectroscopy experiment [12], where an excitation cross section of $\sigma_{\mathrm{exp},3/2^-}=12.0^{+5.3}_{-3.9}$ mb was derived.

In the decay energy spectrum of ^{17}Ne obtained in the present experiment sequential two-proton decays from the second excited state in ^{17}Ne ($J^\pi=5/2^-, E^*=1.764$ MeV) were observed, but no evidence for a simultaneous two-proton decay of the first excited $3/2^-$ state could be found. A lower limit on the lifetime of the two-proton decay of the $3/2^-$ state of $\tau_{2p}>26$ ps was obtained, in agreement with theoretical predictions. Combining the γ and $2p$ spectroscopy information allowed to extract reduced transition probabilities $B(E2)$. The $B(E2)$ values for the excitation of the $3/2^-$ and the $5/2^-$ state in ^{17}Ne could be derived to $B(E2,{}^{17}\mathrm{Ne},1/2^-\rightarrow 3/2^-)=66^{+18}_{-25}$ e^2 fm^4 and $B(E2,{}^{17}\mathrm{Ne},1/2^-\rightarrow 5/2^-)=124\pm 18$ e^2 fm^4, respectively, using the virtual photon method. The measured $B(E2)$ values were compared to shell model calculations in the context of the weak coupling model as well as a model which incorporates core excitations, the latter being in better agreement with experiment.

ACKNOWLEDGMENTS

We acknowledge the contribution of H. Scheit in the development of the drift ellipsoid particle tracking method. One of us (M.J.C.) acknowledges the support and hospitality of the NSCL and the support of the ''Studienstiftung des Deutschen Volkes.'' We thank M. Steiner for producing the radioactive ^{17}Ne beam. This work was supported by the National Science Foundation under Grants No. PHY-007911.

[1] C.N. Davids *et al.*, Phys. Rev. Lett. **76**, 592 (1996).
[2] V.I. Goldanskii, Sov. Phys. JETP **39**, 497 (1960); Nucl. Phys. **19**, 482 (1960); **27**, 648 (1961).
[3] L.V. Grigorenko, R.C. Johnson, I.G. Mukha, I.J. Thompson, and M.V. Zhukov, Phys. Rev. C **64**, 054002 (2001).
[4] D.F. Geesaman *et al.*, Phys. Rev. C **15**, 1835 (1977).
[5] R.A. Kryger *et al.*, Phys. Rev. Lett. **74**, 860 (1995), and references therein.
[6] A. Azhari *et al.*, Phys. Rev. C **58**, 2568 (1998).
[7] I. Muhka *et al.*, Nucl. Phys. **A630**, 394c (1999).
[8] C.R. Bain *et al.*, Phys. Lett. B **373**, 35 (1996).
[9] J. Gómez del Campo *et al.*, Phys. Rev. Lett. **86**, 43 (2001).
[10] V. Guimaraes *et al.*, Phys. Rev. C **58**, 116 (1998).
[11] D.R. Tilley and H.R. Weller, Nucl. Phys. **A564**, 1 (1993).
[12] M.J. Chromik *et al.*, Phys. Rev. C **55**, 1676 (1997).
[13] C.A. Bertulani and G. Baur, Phys. Rep. **163**, 299 (1988).
[14] B.M. Sherrill *et al.*, Nucl. Instrum. Methods Phys. Res. B **70**, 298 (1992).
[15] M.S. Curtin *et al.*, Phys. Rev. Lett. **56**, 34 (1986).
[16] J. Yurkon *et al.*, Nucl. Instrum. Methods Phys. Res. A **422**, 291 (1999).
[17] M.J. Chromik *et al.*, in *Nuclear Structure*, edited by C. Baktash, AIP Conf. Proc. No. 481 (AIP, Woodbury, 1999), p. 187.
[18] M. J. Chromik, Ph.D. thesis, University of Munich, 2001.
[19] S. Kox *et al.*, Nucl. Phys. **A420**, 162 (1984).

[20] R. Schneider, Ph.D. thesis, Technical University Munich, 1996.
[21] E.K. Warburton and B.A. Brown, Phys. Rev. C **46**, 923 (1992).
[22] B.A. Brown *et al.*, Nucl. Phys. **A474**, 290 (1987).
[23] D.W.O. Rogers *et al.*, Nucl. Phys. **A226**, 424 (1974).
[24] A. Ozawa *et al.*, J. Phys. G **24**, 143 (1998).
[25] W. Benenson and E. Kashy, Rev. Mod. Phys. **51**, 527 (1979).
[26] *Table of Isotopes*, 8th ed., edited by R. B. Firestone and V. S. Shirley (Wiley, New York, 1996).
[27] M.J. Chromik *et al.*, in *ENAM98: Exotic Nuclei and Atomic Masses*, edited by B. M. Sherrill, D. J. Morrissey, and C. N. Davids, AIP Conf. Proc. No. 455 (AIP, Woodbury, 1998), p. 286.
[28] F.C. Barker, Phys. Rev. C **63**, 047303 (2001).
[29] L.V. Grigorenko *et al.*, Phys. Rev. Lett. **85**, 22 (2000).
[30] B.A. Brown, Phys. Rev. C **43**, R1513 (1991).
[31] A. Bohr and B. Mottelson, *Nuclear Structure* (World Scientific, Singapore, 1998), Vol. II.
[32] B.A. Brown, A. Arima, and J.B. McGrory, Nucl. Phys. **A277**, 77 (1977).
[33] J.B. McGrory and B.H. Wildenthal, Phys. Rev. C **7**, 974 (1973).
[34] S. Raman *et al.*, At. Data Nucl. Data Tables **36**, 1 (1987).